Supporting Information for

In-Situ g-C_3N_4 Self-Sacrificial Synthesis of g-C_3N_4/$LaCO_3OH$ Heterostructure with Booming Interfacial Charge Transfer and Separation for Photocatalytic NO Removal

Zhenyu Wang [a,b], Yu Huang [b,c*], Long Chen [b,c], Meijuan Chen [a], Junji Cao [a,b,c*], Wingkei Ho [d], Shun Cheng Lee [e]

[a] *School of Human Settlements and Civil Engineering, Xi'an Jiaotong University, Xi'an 710049, China*

[b] *Key Lab of Aerosol Chemistry & Physics, Institute of Earth Environment, Chinese Academy of Sciences, Xi'an 710061, China*

[c] *State Key Lab of Loess and Quaternary Geology (SKLLQG), Institute of Earth Environment, Chinese Academy of Sciences, Xi'an 710061, China*

[d] *Department of Science and Environmental Studies, The Hong Kong Institute of Education, Hong Kong, China*

[e] *Department of Civil and Environmental Engineering, The Hong Kong Polytechnic University, Hung Hom, Hong Kong, China*

**Corresponding author:*

Prof. Yu Huang, E-mail address: huangyu@ieecas.cn Tel: 86-29-6233 6261

Prof. Junji Cao, E-mail address: cao@loess.llqg.ac.cn

Figure Captions

Figure S1. Visible-light photocatalytic activities of CN-LCOH-1.5, CN-LCOH, and CN-LCOH-2.5 for NO removal in air.

Scheme S1. Schematic flow diagram of the photocatalytic test system.

Figure S2. Survey XPS spectra (a) and high-resolution XPS spectra of La 3*d* (b), C 1*s* (c), and N 1*s* (d) of the as-prepared samples.

Figure S3. Energy band structure of CN and LCOH.

Figure S4. The CO_3^{2-} detection experiment.

Figure S5. Visible-light photocatalytic activities of CN and CN after hydrothermal treatment for NO removal in air.

Figure S6. The monitoring of the fraction of ΔNO_2 (a) and NO_2 selectivity of LCOH, CN-LCOH, Mechanical mixture, and CN samples, respectively.

Figure S7. FT-IR spectra of CN-LCOH before and after five photocatalytic repeated reactions.

Figure S8. Schematic crystal structure of (a) g-C_3N_4 (a = 7.153 Å, b = 7.153 Å, c = 7.153 Å), and (b) $LaCO_3OH$ (a = 12.675 Å, b = 12.675 Å, c = 10.081 Å); The crystal models of CN-LCOH (c) before and (d) after geometry optimization.

Figure S9. XRD patterns of (a) g-C_3N_4/$Bi_2O_2CO_3$ and g-C_3N_4 and (b) g-C_3N_4/$SrCO_3$ and g-C_3N_4.

Figure S10. Schematic crystal structure of (a) $Bi_2O_2CO_3$ (a = 3.865 Å, b = 3.862 Å, c = 13.675 Å), and (b) $SrCO_3$ (a = 5.14 Å, b = 8.44 Å, c = 6.11 Å).

Figure S11. Visible-light photocatalytic activities of g-C_3N_4/$Bi_2O_2CO_3$ and g-C_3N_4/$SrCO_3$ for NO removal in air.

Table Caption

Table S1. N element contents, weight ratio LCOH %, weight ratio CN %, molar and weight ratio of $LaCO_3OH$ to the g-C_3N_4 in CN-LCOH-1.5, CN-LCOH, CN-LCOH-2.5, CN-LCOH-1, and CN-LCOH-2.

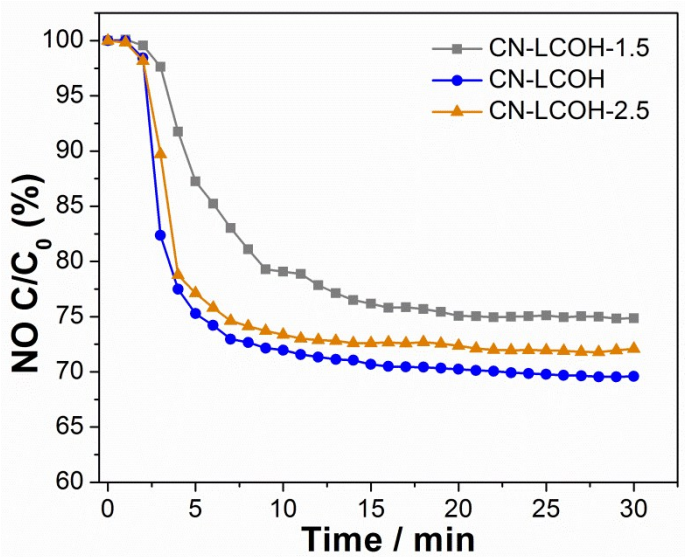

Figure S1. Visible-light photocatalytic activities of CN-LCOH-1.5, CN-LCOH, and CN-LCOH-2.5 for NO removal in air.

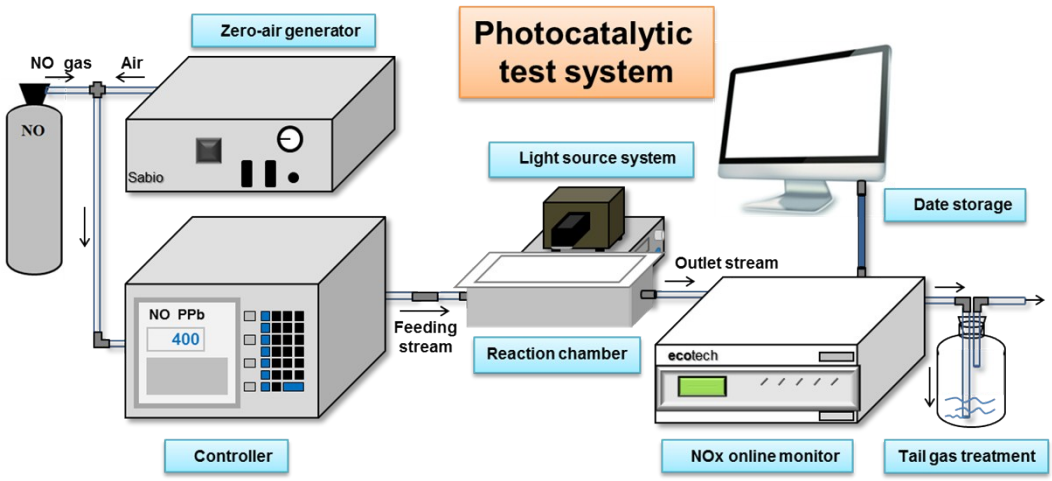

Scheme S1. Schematic flow diagram of the photocatalytic test system

Table S1. N element contents, weight ratio LCOH %, weight ratio CN %, molar and weight ratio of $LaCO_3OH$ to the g-C_3N_4 in CN-LCOH-1.5, CN-LCOH, CN-LCOH-2.5, CN-LCOH-1, and CN-LCOH-2.

Samples	N wt %	Weight ratio LCOH %	Weight ratio CN %	Molar ratio LCOH/CN %	Weight ratio LCOH/CN %
CN-LCOH-1.5	50.20	22.11	77.89	12.09	28.39
CN-LCOH	48.82	24.23	75.77	13.62	31.99
CN-LCOH-2.5	43.72	32.16	67.84	20.19	47.41
CN-LCOH-1	48.65	24.52	75.48	13.83	32.49
CN-LCOH-2	48.53	24.70	75.30	13.97	32.27

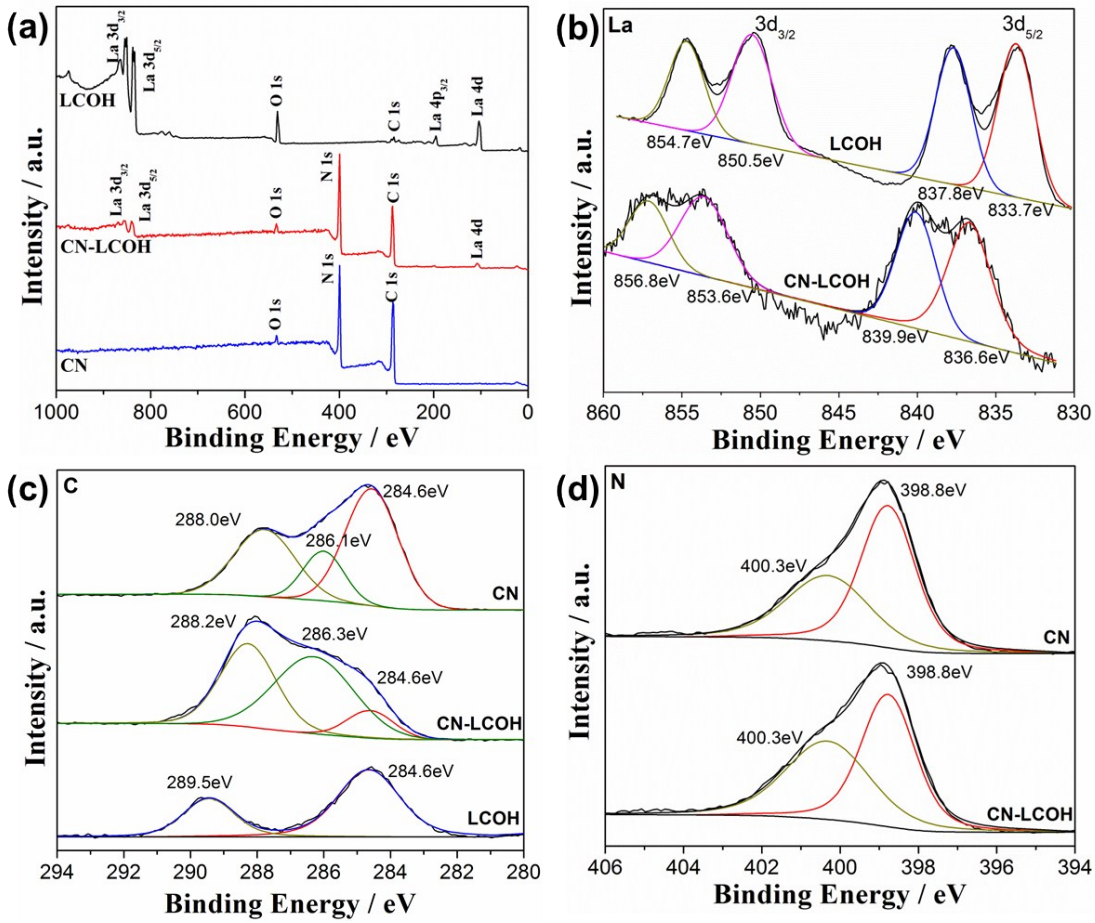

Figure S2. Survey XPS spectra (a) and high-resolution XPS spectra of La 3*d* (b), C 1*s* (c), and N 1*s* (d) of the as-prepared samples.

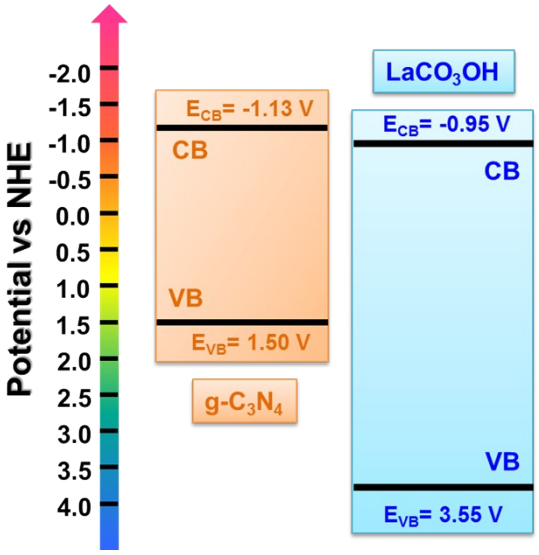

Figure S3. Energy band structure of CN and LCOH.

The generation of CO_3^{2-} from the decomposition of g-C_3N_4 was proved by an experiment as follows:

Repeated the part 2 in experimental section without adding $La(NO_3)_3 \cdot 6H_2O$ at 160 °C for 12h. After cooling down to room temperature naturally, the up-layer clear solutions were added dropwise into 20 mL 0.24 M $BaCl_2$ solution (label 1) and the transparent solution became turbid (Fig. S3a-c). For comparison, deionized water was used instead of the up-layer clear solution and remained other conditions unchanged (label 2). Subsequently, after adding 0.02 M HCl, the turbid solution (label 1) became transparent again and formed amounts of bubbles (Fig. S3d-f), which further illustrated the fact that the CO_3^{2-} do exist in the solution and was generated from the decomposition of g-C_3N_4.

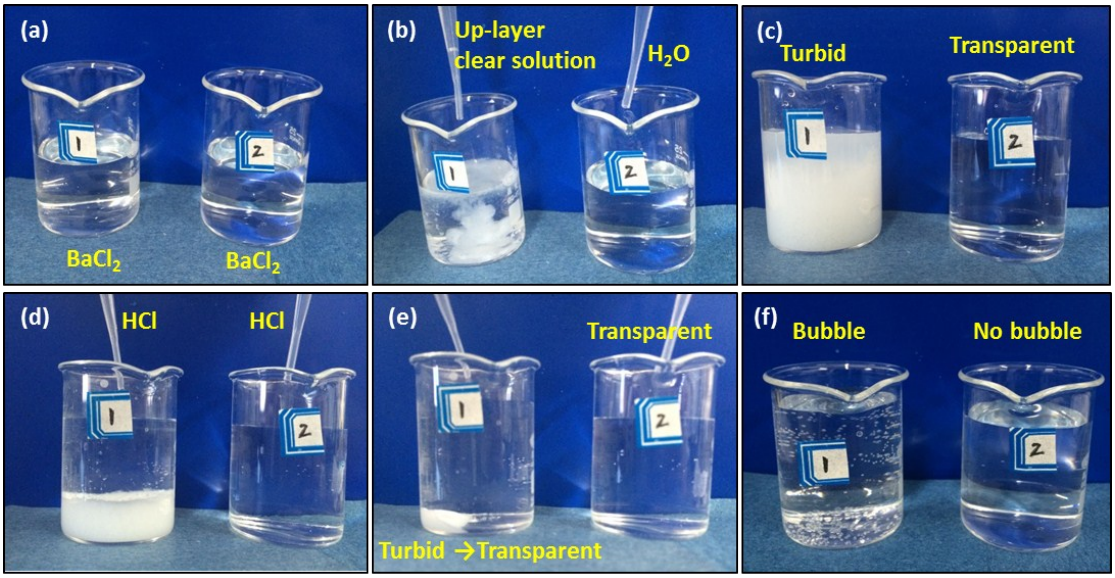

Figure S4. The CO_3^{2-} detection experiment.

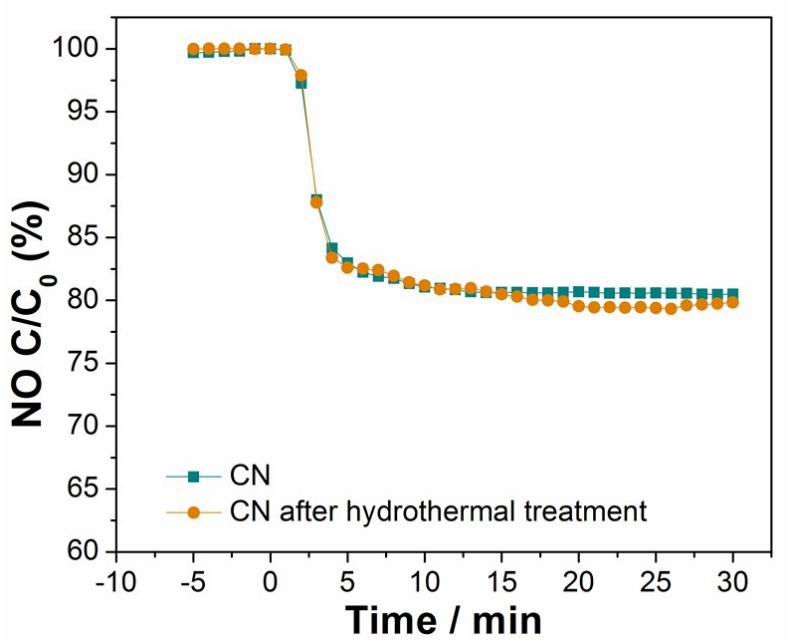

Figure S5. Visible-light photocatalytic activities of CN and CN after hydrothermal treatment for NO removal in air.

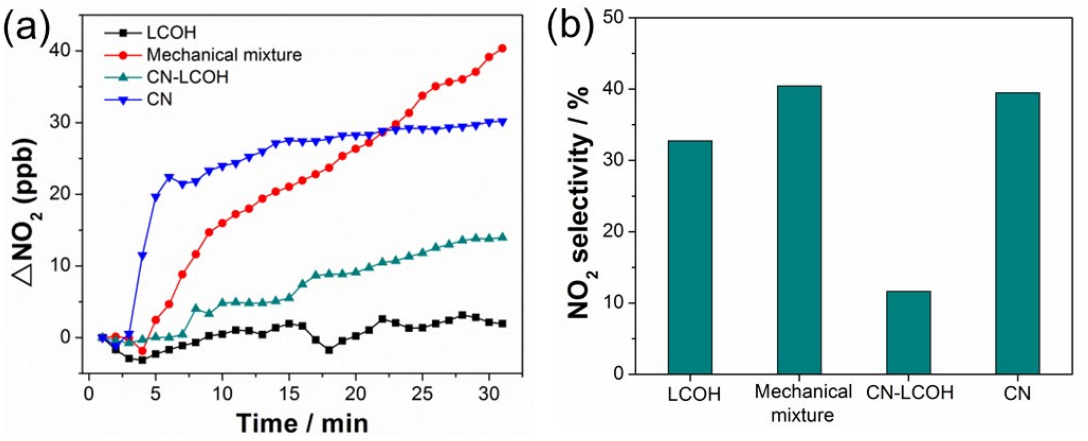

Figure S6. The monitoring of the fraction of ΔNO_2 (a) and NO_2 selectivity of LCOH, CN-LCOH, Mechanical mixture, and CN samples, respectively.

The NO_2 selectivity was calculated according to the following equation [1]:

$$NO_2 \text{ selectivity } (\%) = C_{NO2}/(C_0 - C) \times 100$$

where C_{NO2} represents the production of NO_2, ppb, C_0 is the initial concentration of NO, ppb, and C is the final concentration of NO, ppb.

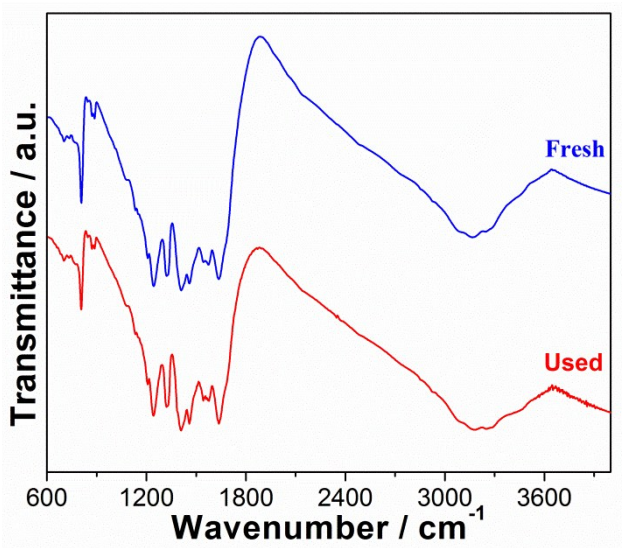

Figure S7. FT-IR spectra of CN-LCOH before and after five photocatalytic repeated reactions.

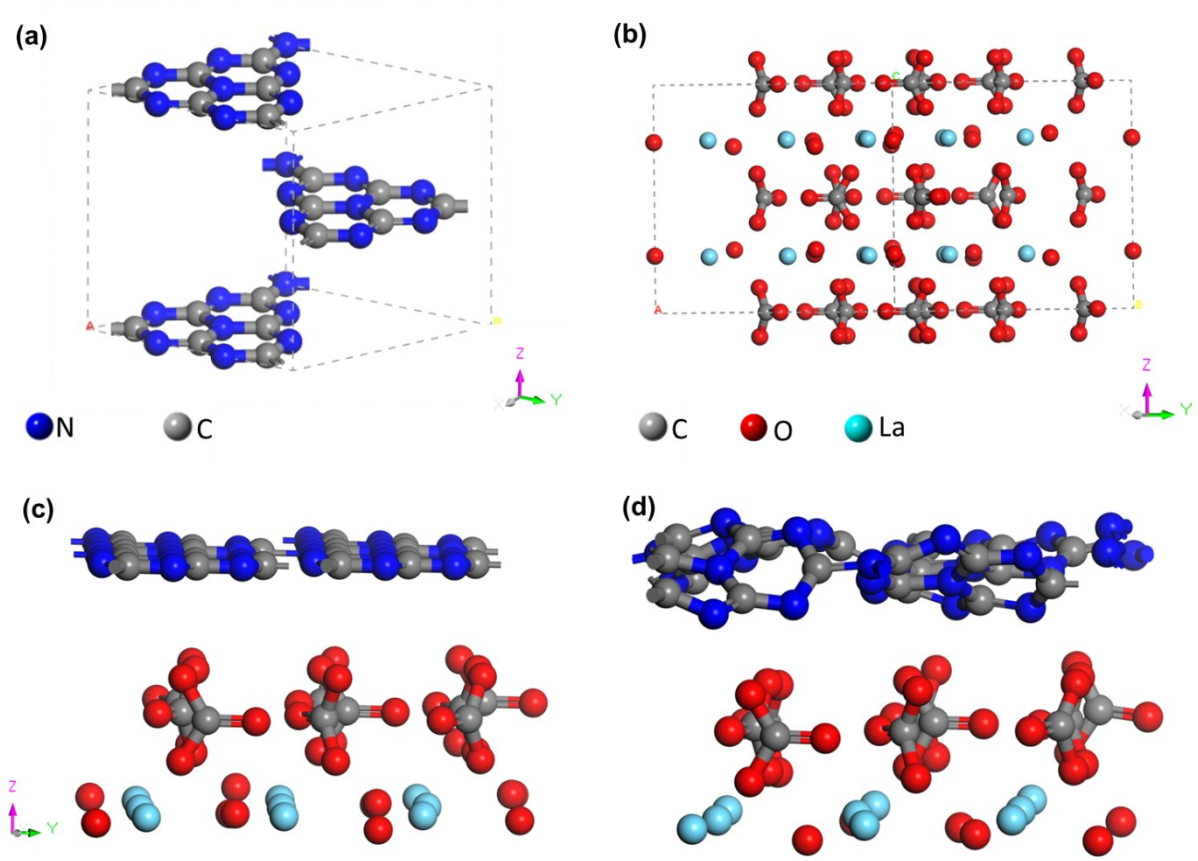

Figure S8. Schematic crystal structure of (a) g-C_3N_4 (a = 7.153 Å, b = 7.153 Å, c = 7.153 Å), and (b) $LaCO_3OH$ (a = 12.675 Å, b = 12.675 Å, c = 10.081 Å); The crystal models of CN-LCOH (c) before and (d) after geometry optimization.

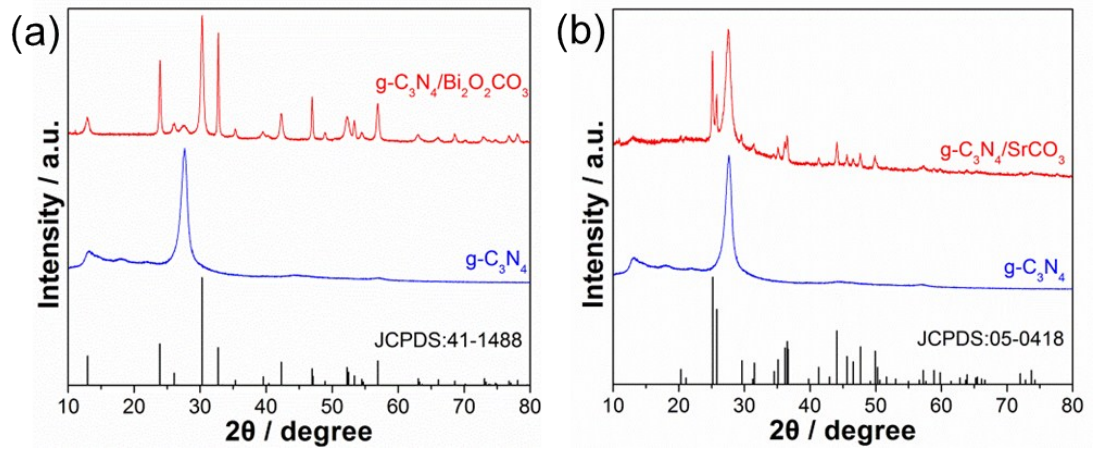

Figure S9. XRD patterns of (a) g-C_3N_4/$Bi_2O_2CO_3$ and g-C_3N_4 and (b) g-C_3N_4/$SrCO_3$ and g-C_3N_4.

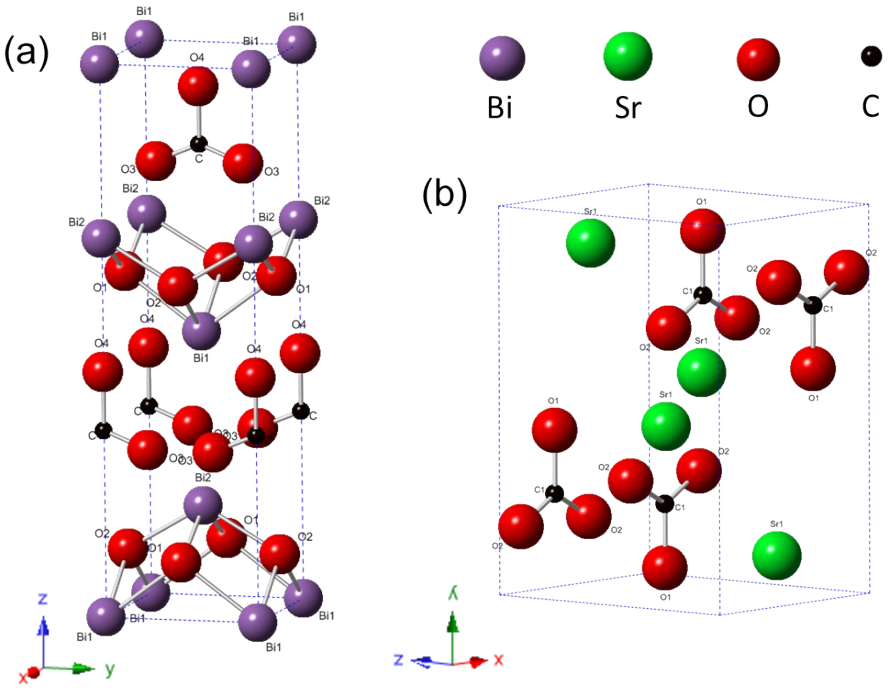

Figure S10. Schematic crystal structure of (a) $Bi_2O_2CO_3$ (a = 3.865 Å, b = 3.862 Å, c = 13.675 Å), and (b) $SrCO_3$ (a = 5.14 Å, b = 8.44 Å, c = 6.11 Å).

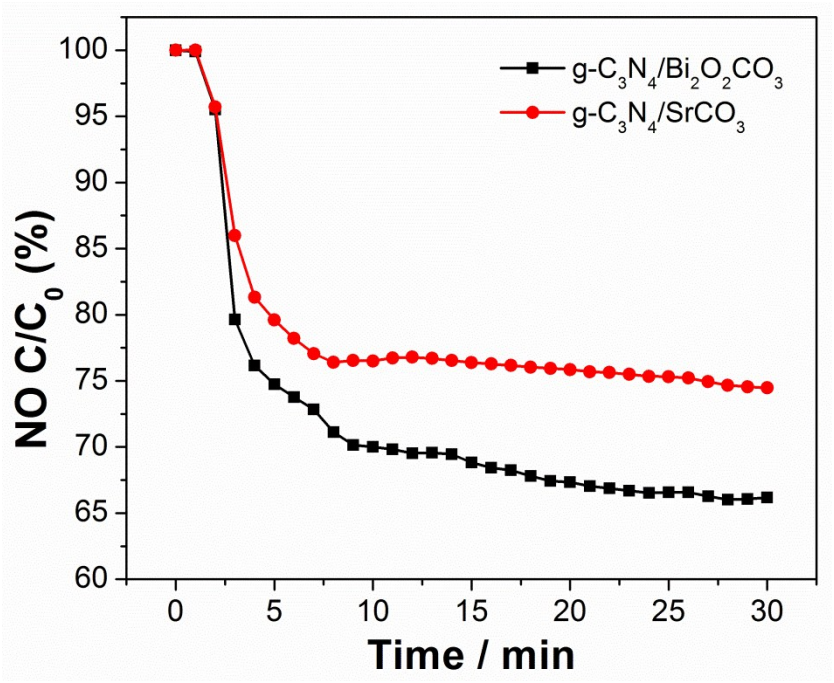

Figure S11. Visible-light photocatalytic activities of g-C_3N_4/$Bi_2O_2CO_3$ and g-C_3N_4/$SrCO_3$ for NO removal in air.

1 J. Ma; C. Wang; H. He, *Appl. Catal. B: Environ.,* 2016*,* **184**, 28-34.